International Journal of Heat and Mass Transfer 66 (2013) 31–45

Contents lists available at SciVerse ScienceDirect

International Journal of Heat and Mass Transfer

journal homepage: www.elsevier.com/locate/ijhmt

Flow condensation in horizontal tubes

Hyoungsoon Lee [a], Issam Mudawar [a,*], Mohammad M. Hasan [b]

[a] Boiling and Two-Phase Flow Laboratory (BTPFL), School of Mechanical Engineering, Purdue University, 585 Purdue Mall, West Lafayette, IN 47907, USA
[b] NASA Glenn Research Center, 21000 Brookpark Road, Cleveland, OH 44135, USA

ARTICLE INFO

Article history:
Received 30 April 2013
Received in revised form 20 June 2013
Accepted 20 June 2013
Available online 27 July 2013

Keywords:
Condensation
Horizontal flow
Interfacial waves

ABSTRACT

This study examines condensation heat transfer in horizontal channels. Two separate condensation modules are tested using FC-72 as condensing fluid and water as coolant. The first module is dedicated to obtaining detailed heat transfer measurements of the condensing flow, and the second to video capture of the condensation film's interfacial behavior. Four dominant flow regimes are identified: smooth-annular, wavy-annular, stratified-wavy and stratified, whose boundaries show fair agreement with published flow regime maps. The film's interface is observed to feature an array of small ripples and relatively large waves, with the largest waves tending to merge into yet larger waves having greater liquid mass, amplitude and speed. This behavior is believed to influence condensation heat transfer, especially downstream. The local condensation heat transfer coefficient is highest near the inlet, where quality is near unity and the film thinnest, and decreases monotonically in the axial direction in response to the film thickening. This variation is very sensitive to the mass velocity of FC-72, and the heat transfer coefficient decreases sharply in the inlet region but this decrease slows significantly in the downstream region because of the combined effects of turbulence and interfacial waviness. The measured condensation heat transfer coefficient shows good agreement with a select number of correlations.

1. Introduction

Phase change processes play a crucial role in the operation of power generation, chemical, pharmaceutical and heating and air conditioning systems. However, newer applications have emerged during the past three decades whose performance is highly dependent on the ability to dissipate large amounts of heat within limited volume. These include computer data centers, hybrid vehicle power electronics, avionics, lasers, and X-ray medical devices [1]. These applications have created a need to adapt two-phase processes into compact configurations that promise several orders-of-magnitude enhancement in evaporation and condensation heat transfer coefficients compared to those possible with single-phase liquid cooling alone. This shift is manifest in the surge of studies concerning virtually all possible evaporation and flow boiling configurations, including pool boiling [2,3], channel flow boiling [4,5], jet [6–8] and spray [9,10], as well as enhanced surfaces [11,12] and hybrid cooling configurations [13,14].

But heat acquisition constitutes only part of the challenge. Often achieved with the aid of a closed two-phase flow loop, heat acquisition by evaporation or flow boiling requires commensurate heat rejection capability that relies mostly on condensation. There is therefore a need for design tools for high performance condensation hardware, with particular emphasis on increasing the ratio of heat dissipation rate to pressure drop.

For internal condensing flows with superheated vapor inlet conditions, condensation is initiated with the formation of a thin liquid film along the inner walls of the tube, which marks the initiation of the annular flow regime. Axial thickening of the wavy condensate film ultimately causes wave crests from diametrically opposite sides of the tube to merge, which commences formation of the slug flow regime. Continued axial condensation causes a reduction in the length of the slug flow bubbles. The bubbly flow regime is initiated where the length of the slug flow bubbles drops below the tube diameter. Eventually, the flow is converted to pure liquid. Among these flow regimes, annular flow is by far the most important because it is typically prevalent over a large fraction of the condensation length, and its ability to provide the highest condensation heat transfer coefficients. This explains the emphasis researchers place on the annular regime compared to all other regimes combined.

Predicting pressure drop and heat transfer in annular condensing flows relies on (a) semi-empirical correlations [15–18], whose applicability is limited to fluids and operating conditions of specific databases, (b) universal correlations [19,20], which are derived from consolidated databases for many types of fluids and covering broad ranges of geometrical and flow parameters, and (c) theoretical control-volume-based models [21,22].

* Corresponding author. Tel.: +1 (765) 494 5705; fax: +1 (765) 494 0539.
E-mail address: mudawar@ecn.purdue.edu (I. Mudawar).
URL: https://engineering.purdue.edu/BTPFL (I. Mudawar).

0017-9310/$ - see front matter © 2013 Elsevier Ltd. All rights reserved.
http://dx.doi.org/10.1016/j.ijheatmasstransfer.2013.06.044

Nomenclature

Bo	bond number
$C_{D,w}$	drag coefficient on wave
c_p	specific heat at constant pressure
D, D_i	inner diameter of condensation tube
D_h	hydraulic diameter
D_o	outer diameter of condensation tube
G	mass velocity of FC-72
g	gravitational acceleration
G_w	mass velocity of water
h	local condensation heat transfer coefficient
$\bar{h}$	average condensation heat transfer coefficient
h_{fg}	latent heat of vaporization
j	superficial velocity
j^*	dimensionless superficial velocity
j_g'	modified superficial vapor velocity
k	thermal conductivity
$\dot{m}$	mass flow rate
MAE	mean absolute error
P	pressure
P_R	reduced pressure, $P_R = P/P_{crit}$
Pr	Prandtl number
q''	heat flux
Re	Reynolds number
Re_{eq}	equilibrium Reynolds number
T	temperature
T^+	dimensionless temperature
u_w	wave velocity
v^*	shear velocity
W	outer channel width of condensation module CM-FV
We	Weber number
We^*	modified Weber number
X	vapor quality
x_e	thermodynamic equilibrium quality
X_{tt}	Lockhart–Martinelli parameter
Z	stream-wise coordinate

Greek symbols

δ^+	dimensionless film thickness
μ	dynamic viscosity
ρ	density
σ	surface tension
ϕ	two-phase pressure drop multiplier

Subscripts

air	air
crit	critical pressure
exp	experimental
f	saturated liquid
FC	FC-72
film	liquid film
fo	liquid only
fr	frictional
g	saturated vapor
i	inner surface of condensation tube
in	inlet of condensation length
o	outer surface of condensation tube
pred	predicted
sat	saturation
ss	stainless steel
tt	turbulent liquid – turbulent vapor
w	water
wall	wall

One useful tool investigators often rely upon to aid the prediction of condensing flows is the use of flow regime maps. By pinpointing the dominant flow regime, they are better able to tailor models to this particular regime. Several types of flow regime maps have been recommended, which employ different coordinates to segregate flow regimes, such as mass velocity versus quality [17,23,24], and superficial velocity of vapor, j_g, versus that of liquid, j_f [25,26]. Large disagreements in the predictions of regime maps for different working fluids has lead some to incorporate dimensionless groups, such as j^*, X_{tt} and We^*, that are more effective at capturing the dominant forces associated with different regimes [27,28]. A key drawback to flow regime maps in general is the difficulty representing the many dimensionless groups governing multiple flow regimes using a single two-dimensional plot.

The present study is a part of a long-term NASA-supported initiative to develop the Flow Boiling and Condensation Experiment (FBCE), which is scheduled for future deployment in the International Space Station (ISS). This initiative is rooted in the realization that, despite the few useful published studies concerning flow boiling and condensation in microgravity [29–33], the corresponding databases and reliable predictive tools are quite sparse. The overall objectives of the NASA initiative are to (i) obtain flow boiling and condensation databases in microgravity, (ii) develop mechanistic models for flow boiling and condensation, and (iii) determine the minimum flow rate required to ensure gravity-independent cooling. A key tactic in assessing the influence of gravity is to compare data from experiments that are conducted separately in microgravity and Earth's gravity. The present study explores horizontal flow condensation at Earth's gravity. First, video motion analysis is used to explore both the interfacial behavior of the condensing film and longitudinal transitions between condensation regimes. Secondly, detailed heat transfer measurements are made to ascertain the axial variations of the condensation heat transfer coefficient in response to variations in mass velocities of the condensing fluid and cooling water. Results are then compared to predictions of flow regime maps and popular correlations for the condensation heat transfer coefficient.

2. Experimental methods

2.1. Condensation facility

The condensation facility constructed for this study is designed to condense FC-72 by rejecting heat to water. Fig. 1(a) shows this facility consists of two separate sub-loops, one for FC-72 and the other for the cooling water, and an accessory that is used for FC-72 deaeration. As depicted in Fig. 1(b), the components of the facility are segregated into three separate rigs: (i) the main condensation rig, (ii) water conditioning rig, and (iii) deaeration rig.

In the FC-72 sub-loop, the FC-72 is circulated with the aid of a magnetically driven Micropump GB gear pump, followed by a flow control valve, filter, and Flow Technology FTO-3 turbine flow meter. The FC-72 is the heated through a CAST-X 3000 circulation heater to a quality slightly higher than unity before entering one of two condensation modules that are described below. Exiting the

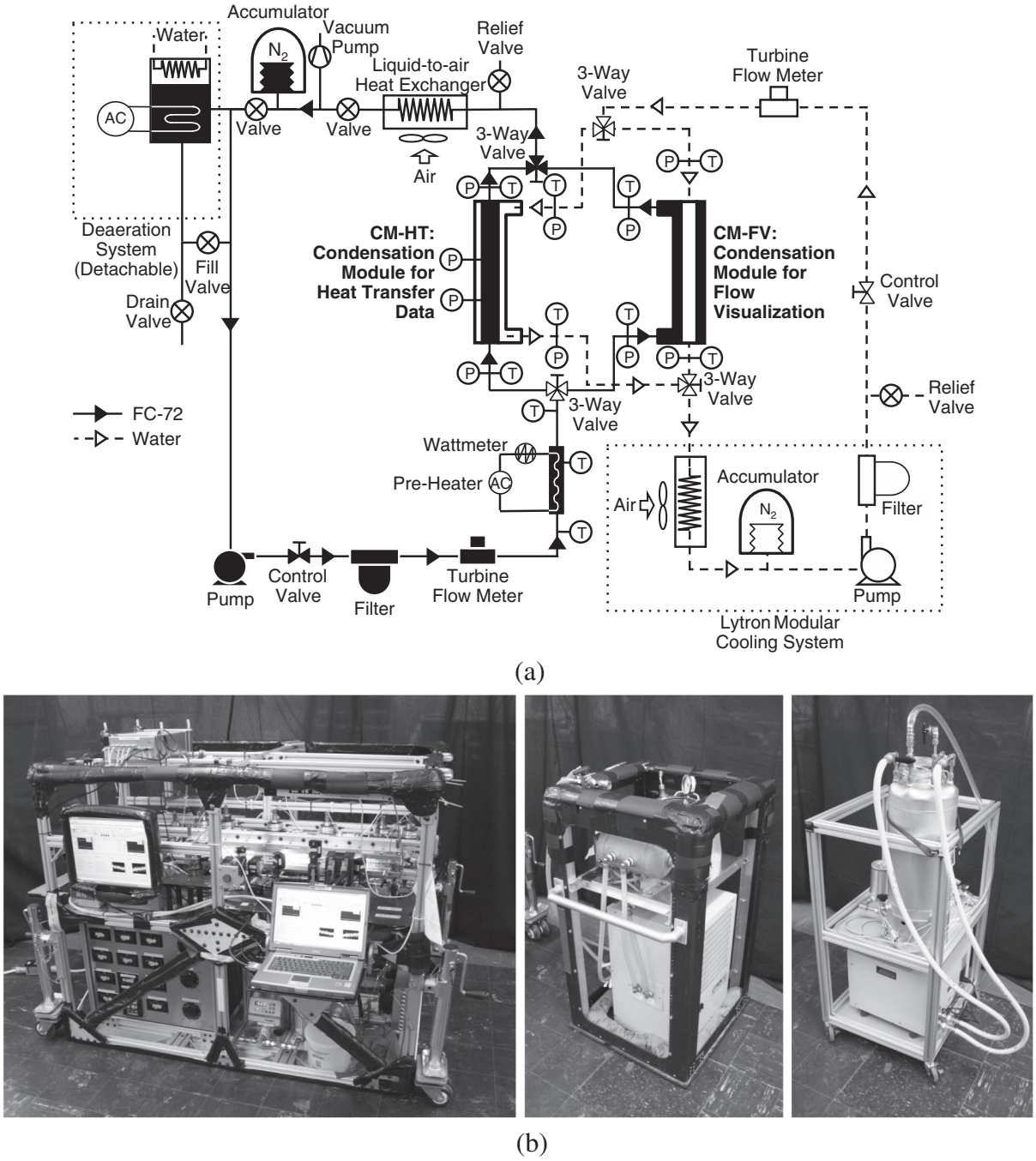

Fig. 1. (a) Schematic of flow loop. (b) Photos of main condensation rig, water conditioning rig, and deaeration rig.

selected condensation module, the FC-72 two-phase mixture is passed through a Lytron liquid-to-air heat exchanger to convert it to pure liquid. Pressure in the FC-72 sub-loop is controlled by a pre-set nitrogen gas pressure in a Flexicraft accumulator, which contains metallic bellows to accommodate any fluctuations in FC-72 volume due to phase change. All components of the FC-72 sub-loop are contained in the main condensation rig. Also contained in the same rig are a laptop, data acquisition system, pressure, temperature, and flow rate display panels, and both FC-72 and water control valves.

The water sub-loop is separately controlled to reject the heat from the FC-72 vapor to achieve condensation in the selected condensation module. The water is circulated with the aid of a Lytron system containing a pump and a fan-cooled heat exchanger that is modified with a stainless steel reservoir. Like the FC-72 sub-loop, pressure in the water sub-loop is set by a Flexicraft accumulator. The flow rate of water supplied to the selected condensation module is regulated with a control valve and measured by a Flow Technology FTO-4 turbine flow meter. Exiting the condensation module, the water is returned to the Lytron system, where it is cooled to near-ambient temperature.

The FC-72 is carefully deaerated before performing any series of tests. The deaeration rig contains four immersion heaters and a condensation coil that is cooled by a secondary water source using a liquid–air Lytron cooling system. The FC-72 is simultaneously boiled and condensed for 30 min before being charged into the FC-72 sub-loop. When the deaerated FC-72 is supplied into the flow loop, it comes in contact with air inside the flow loop. So,

the FC-72 is recirculated three to four times until the entire loop is filled with deaerated FC-72.

2.2. Condensation modules

This study employs two separate condensation modules. Reasons behind the need for the two modules will be explained later. Shown in Fig. 2(a)–(d), the first condensation module, CM-HT, is used for acquiring detailed heat transfer measurements for FC-72 condensing through a circular 304 stainless steel tube having a 7.12-mm i.d., 0.41-mm wall thickness and 791.71-mm condensation length. The FC-72 is cooled by a counterflow of water through a 12.7-mm o.d. annulus. The small wall thickness of the inner stainless steel tube is intended to minimize axial conduction effects. The FC-72 vapor enters CM-HT through the left header depicted in Fig. 2(a) and (b), which is fitted with an aluminum honeycomb flow straightener. The water is introduced from the right header. Both ends of the stainless tube are fitted with fiberglass plastic (G-10) sleeves to minimize heat loss beyond the intended condensation length. The sleeves have 6.8-degree tapered edges to minimize any wake effects at the ends of the condensation length. At both headers of CM-HT, the FC-72 and water temperatures and pressures are measured using type-T thermocouples and Honeywell STJE absolute pressure transducers, respectively. The outer wall temperatures of the stainless steel tube are measured by 36-gauge, type-T thermocouples at 15 axial locations along the condensation length. At each axial location, up to four thermocouples are distributed circumferentially 90° apart to check for circumferential asymmetry. Of 54 outer wall thermocouple locations, 30 are actually populated. The water temperatures are measured at the same 15 axial locations as the stainless steel tube's outer wall thermocouples using pairs of type-T thermocouples inserted into the water flow 180° apart with the aid of miniature stainless steel tubes. The material surrounding the water annulus in CM-HT is thermally insulating polycarbonate plastic (Lexan), which is intended to minimize heat loss to the ambient.

The circular geometry of the inner tube of CM-HT is ideally suited for comparisons with theoretical condensation models. However, this geometry precludes optical access to the condensation film. Therefore, a second condensation module, CM-FV, is used entirely for flow visualization purposes. The FC-72 and water flows in CM-FV are reversed compared to CM-HT. As shown in Fig. 3(a)–(d), the water flow in CM-FV is passed through a 304 stainless steel tube having a 5.99-mm o.d., 0.254-mm wall thickness, and a total condensation length of 777.24 mm. The FC-72 flows in the opposite direction through an annulus between the stainless steel tube and outer channel walls made from polycarbonate plastic (Lexan). Unlike CM-HT, the outer surface of the annulus in CM-FV is square, Fig. 3(a), to provide unobstructed optical access to the FC-72 film condensing along the outer wall of the stainless steel tube. The perimeter of the outer surface of the annulus of CM-FV is carefully selected to achieve a hydraulic diameter for the FC-72 flow of 7.12 mm, equal to that in CM-HT. At both headers of CM-FV, the FC-72 and water temperatures and pressures are measured with type-T thermocouples and Honeywell STJE absolute pressure transducers, respectively. An aluminum honeycomb insert and G-10 insulating sleeve are location in the FC-72 inlet.

A FASTCAM-Ultima APX high-speed camera is used to capture interfacial characteristics of the condensate film and dominant flow regimes at three locations along the condensation length of

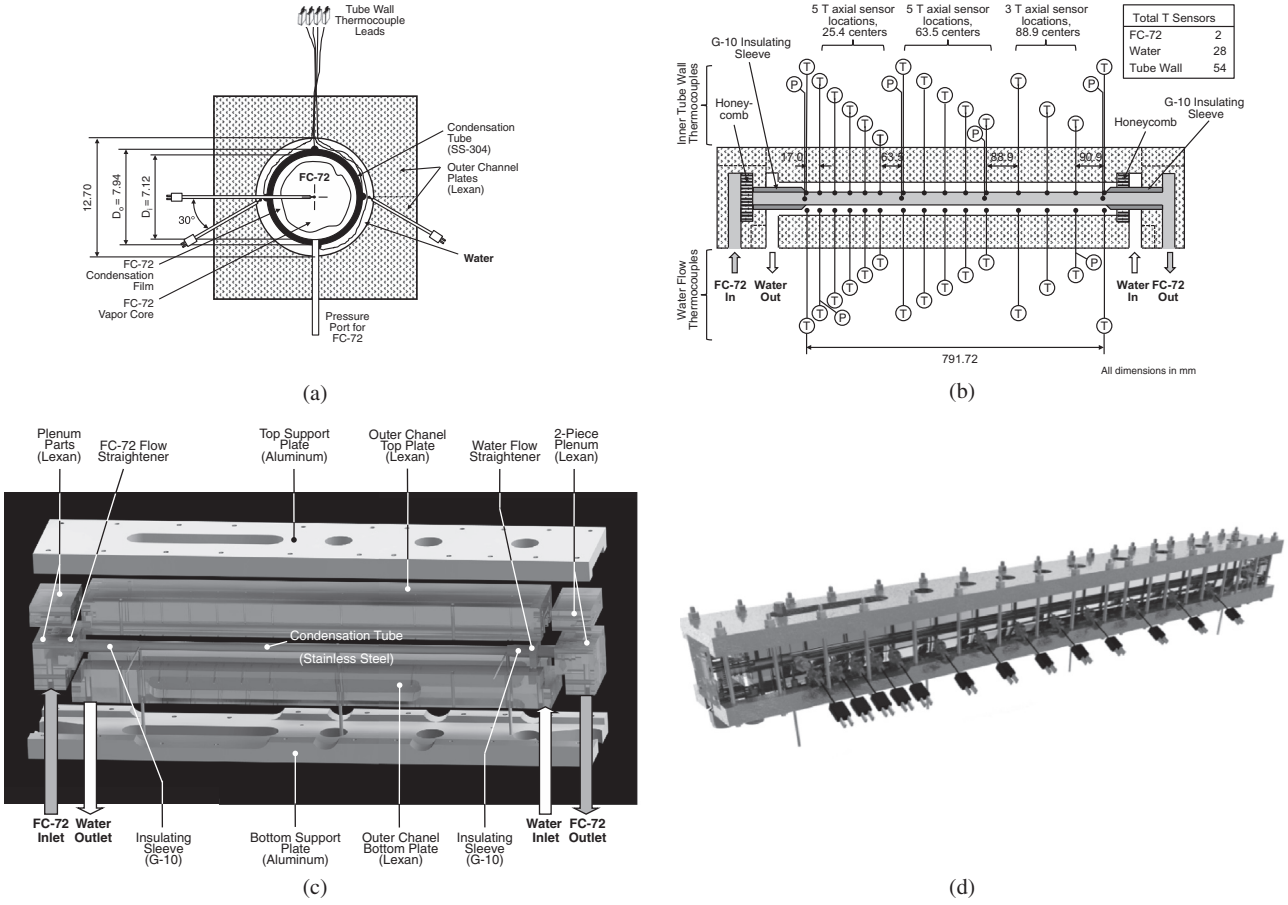

Fig. 2. Construction of condensation module CM-HT for heat transfer measurements: (a) cross-sectional diagram, (b) longitudinal sectional diagram, (c) CAD model of module parts, and (d) CAD model of module assembly with instrumentation.

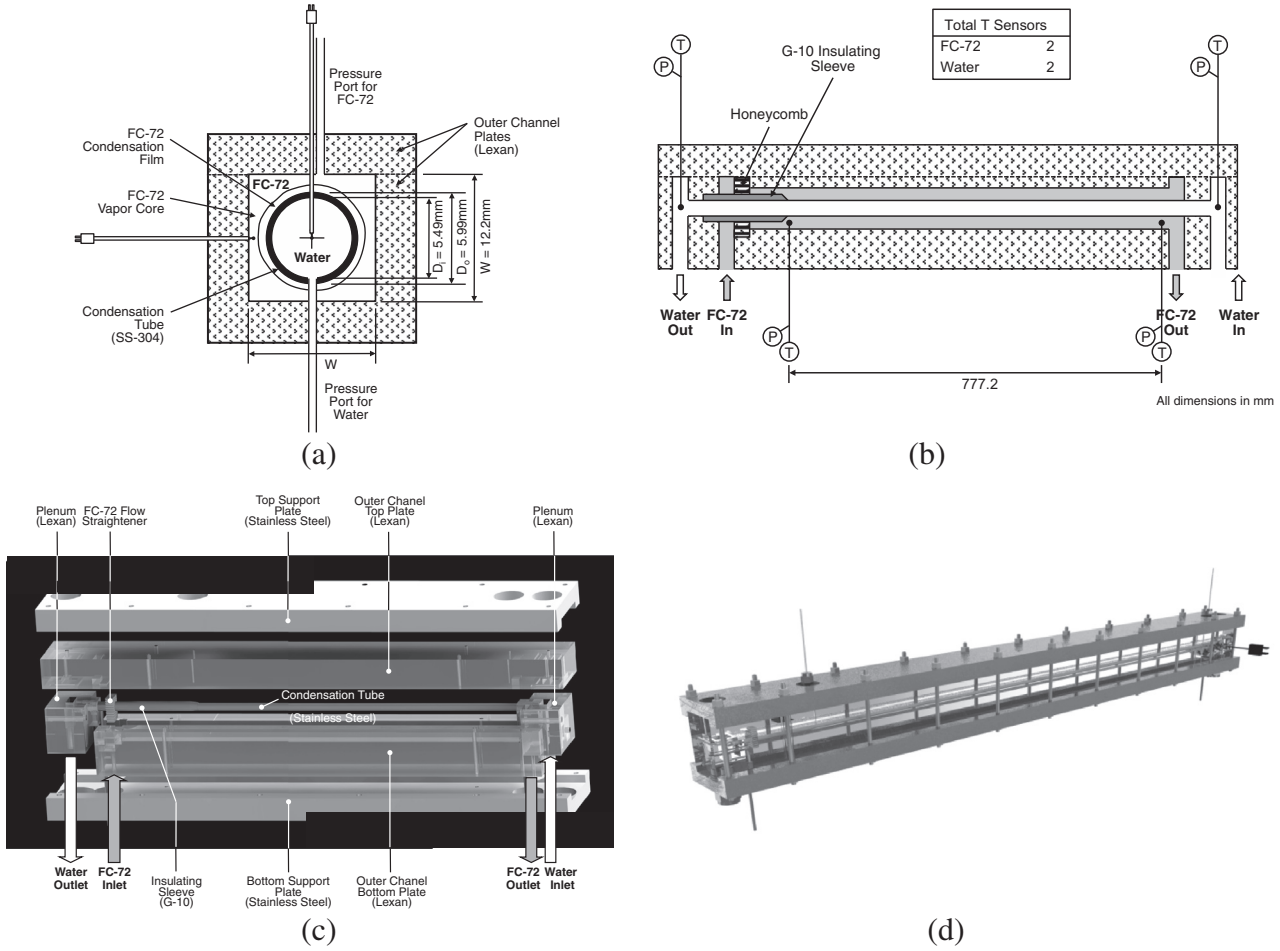

Fig. 3. Construction of condensation module CM-FV for flow visualization: (a) cross-sectional diagram, (b) longitudinal sectional diagram, (c) CAD model of module parts, and (d) CAD model of module assembly with instrumentation.

CM-FV. All images presented in this study were captured at 6000 frames per second; individual images are 20-mm long and centered at 65, 263 and 561 mm from the inlet of the condensation length, representing, respectively, the inlet, middle and outlet regions of the condensing FC-72 flow. The video records are captured for 0.75 s with 512 × 512-pixel resolution. Lighting for the video camera is achieved by 16 of 5-W white LEDs, which are fitted with a cooling fan.

2.3. Operating conditions and measurement uncertainty

The operating conditions for the present study are as follows: FC-72 mass velocity of $G = 143.0–402.4$ kg/m^2 s, FC-72 inlet pressure of $P_{FC,in} = 101.7–131.7$ kPa (14.8–19.1 psia), FC-72 saturation temperature of $T_{sat} = 56.7–64.7$ °C, FC-72 inlet thermodynamic equilibrium quality of $x_{e,in} = 1.00–1.05$, water mass velocity of $G_w = 294.3–487.8$ kg/m^2 s, water inlet pressure of $P_{w,in} = 114.8–126.2$ kPa (16.7–18.3 psia), and water inlet temperature of $T_{w,in} = 25.2–28.7$ °C. The highest FC-72 film Reynolds number achieved is $Re_{film} = 4260.3$. Table 1 provides a summary of the thermophysical properties of FC-72 at $T_{sat} = 62$ °C.

Pressures throughout the condensation facility are measured by Honeywell STJE absolute pressure transducers with an accuracy of ±0.05%. The temperatures are measured with type-T thermocouples having an uncertainty of ±0.4 °C. The Flow Technology Omniflo turbine flow meters used to measure the flow rates of FC-72 and water possess an accuracy of ±0.25%. The maximum uncertainties in determining the equilibrium quality and condensation heat transfer coefficient are ±10.05% and ±11.12%, respectively.

Table 1
Thermophysical properties of saturated FC-72 at 62 °C ($P = 1.21$ bar).

k_f [W/m K]	μ_f [kg/m s]	$c_{p,f}$ [J/kg K]	σ [mN/m]	h_{fg} [kJ/kg]	ρ_f [kg/m^3]	ρ_g [kg/m^3]
0.0532	409×10^{-6}	1,110	7.8	93.03	1,578	15.86

3. Flow visualization results from CM-FV

3.1. Interfacial behavior and dominant flow regimes

Fig. 4 shows sequential images of the FC-72 film condensing on the outer wall of the horizontal stainless steel tube in CM-FV for five FC-72 mass velocities of $G = 115.8$, 83.0, 65.6, 49.2 and 33.4 kg/m^2 s and a narrow range of water mass velocities of $G_w = 845.5–854.2$ kg/m^2 s. Shown are sequences for the inlet, middle and outlet regions, with individual images in each sequence separated by 0.005 s. Quality values are based on the assumption of linear variation of x_e with z between $x_e = 1$ for $z = 0$ and computed outlet quality; the x_e values indicated in Fig. 4 are averaged over the length of the respective region. In each case, the FC-72 enters the annulus in pure vapor state, and the condensation film begins to form in the inlet region and thickens axially, with gravity

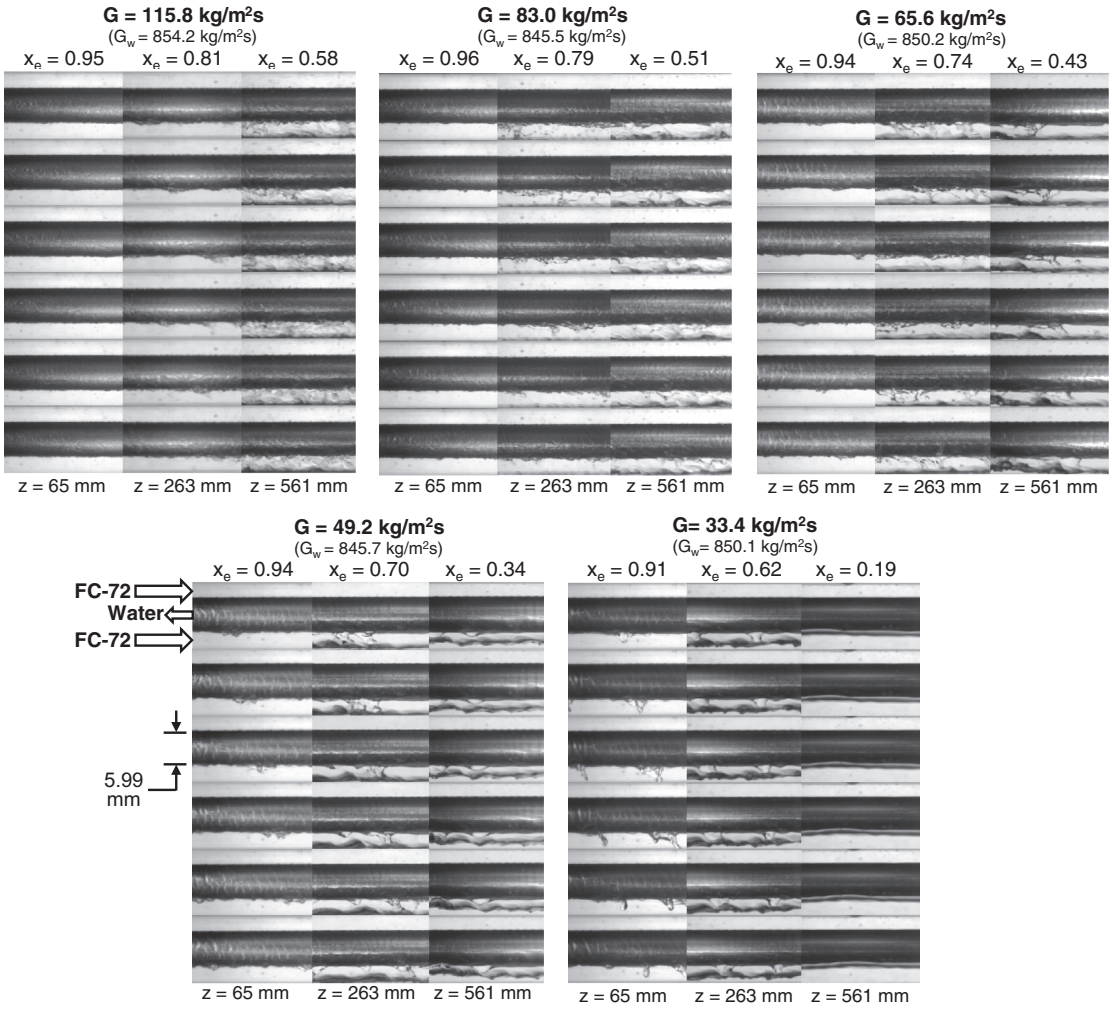

Fig. 4. Sequential images of horizontal flow condensation on outer surface of stainless steel tube captured in upstream, middle and downstream regions of CM-FV centered at 65, 263 and 561 mm, respectively, from inlet of condensation length for FC-72 mass velocities of G = 115.8, 83.0, 65.6, 49.2 and 33.4 kg/m^2 s and narrow range of G_w (845.5–854.2 kg/m^2 s). Individual images in each sequence are separated by 0.005 s, and the indicated values of x_e are averaged over each region.

causing appreciable thickening on the tube's underside. It should be noted that the shear stress exerted by the vapor on the film interface is greatest in the inlet region and decreases monotonically in the axial direction because of the flow deceleration associated with the condensation. As discussed below, four distinct flow regimes are identified: *smooth-annular*, *wavy-annular*, *stratified-wavy* and *stratified*, with their occurrence depending mostly on the mass velocity of FC-72.

It should be noted that interfacial waves are known to have a profound influence on the transport behavior of adiabatic films [34,35], films subjected to sensible heating [36–38], and evaporating films [39]. The present flow visualization experiments point to equally important role of waves in condensing flows.

The *smooth-annular* flow regime, which is characterized by a thin and fairly smooth liquid film, is observed in the inlet region for the two highest FC-72 mass velocities of G = 115.8 and 83.0 kg/m^2 s. For the same flow rates, the film becomes thicker downstream with noticeable interfacial waviness, especially along the tube's underside, where the film flow can be best categorized as *wavy-annular*. Notice that the flow atop the tube is very thin as much of the liquid in the middle and outlet regions is drained downwards. This also causes some of the liquid to break from the film, especially in the outlet region, and accumulate in the channel beneath the tube, a process that is made possible by the axial decrease in vapor shear. The *wavy-annular* regime is encountered in the inlet region for the three lower FC-72 mass velocities of G = 65.6, 49.2 and 33.4 kg/m^2 s, accompanied by underside thickening in the same region because of weaker vapor shear for these mass velocities even in the inlet region. Appreciable drainage and accumulation of liquid, which can be best characterized as *stratified-wavy*, is observed in the middle and outlet regions for G = 83.0, 65.6 and 49.2 kg/m^2 s, and middle region for G = 33.4 kg/m^2 s. The outlet region for G = 33.4 kg/m^2 s is dominated by *stratified* flow beneath the tube with a fairly smooth interface, which can be explained by both the low vapor quality of 0.19 and comparatively very low vapor shear. The vapor shear stress in this case appears too weak to even perturb the interface of the liquid layer beneath.

An interesting and recurring aspect of interfacial behavior of the film on the tube's underside is merging of adjacent waves into a single larger, and faster moving wave. This is shown for the inlet region with G = 49.3 kg/m^2 s in Fig. 5(a). Fig. 5(b) shows a schematic of this phenomenon for an upstream wave 1 and downstream wave 2. Because of the large protrusion of these waves into the vapor flow, they each cause separation of the faster vapor flow upstream. A net mostly form drag force associated with a drag coefficient $C_{D,w}$ is induced on the upstream front of each wave, resulting in wave speed u_w. For somewhat similar interfacial

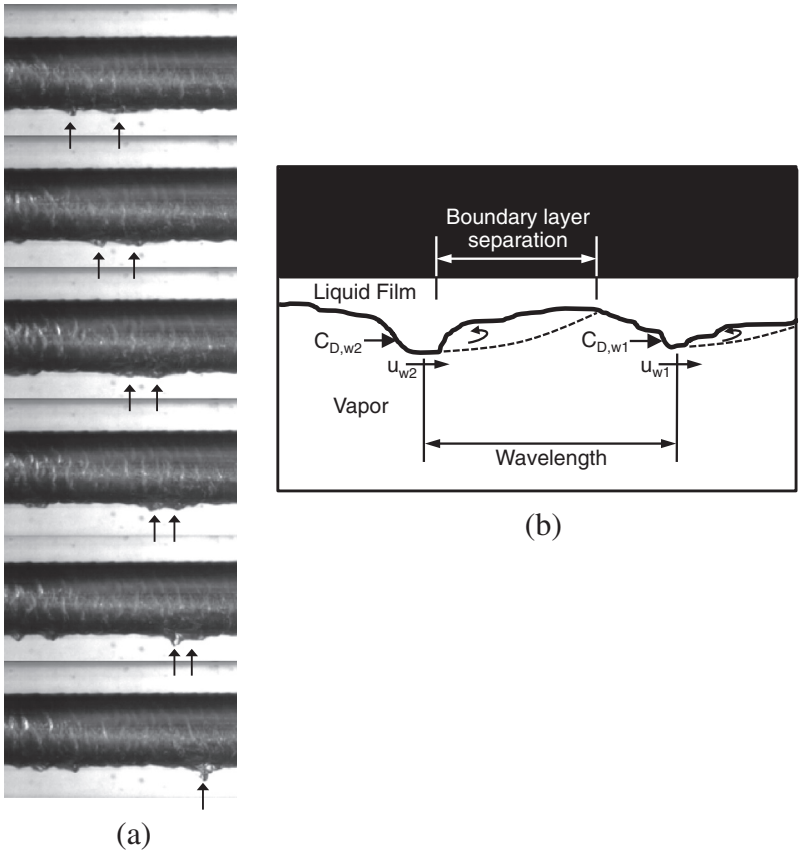

Fig. 5. (a) Sequential images of the condensate film along outer surface of the stainless steel tube in CM-FV depicting wave merging in the inlet region for $G = 49.3$ kg/m^2 s, $G_w = 844.7$ kg/m^2 s and $x_e = 0.94$; individual images are centered at $z = 65$ mm and separated by 0.004 s. (b) Schematic of drag induced wave merging.

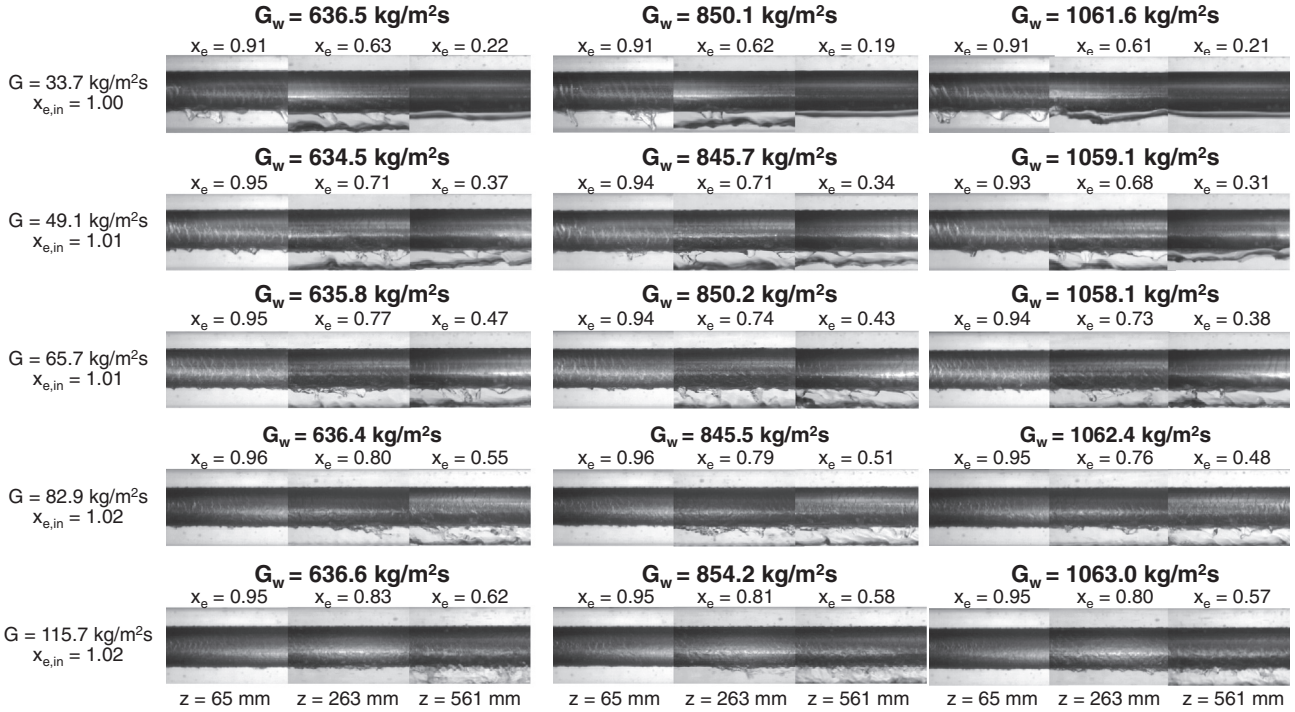

Fig. 6. Images of horizontal flow condensation on outer surface of stainless steel tube captured in upstream, middle and downstream regions of CM-FV for three narrow ranges of water mass velocity and five FC-72 mass velocities.

Table 2
Details of prior flow regime maps.

	Mandhane et al. [25]	Breber et al. [43]	Soliman [23,24]	Wang et al. [17]	Cavallini et al. [28]	Chen et al. [41]	Kim and Mudawar [42]
Working fluid	Air–water	R11, R113, R12, *n*-pentane, steam	Steam, R113, R12	R134a	R125, R134a, R22, R236ea, R32, R410A	R134a	FC-72
D_h [mm]	12.7–165.1	4.8–50.8	7.4–12.7	1.46	8	12, 14	1
Quality range	–	–	0.2–0.95	0.03–0.94 (inlet quality)	–	–	0–1

protrusions, the drag coefficients and speeds of the two waves are fairly equal, provided they are separated by a large wavelength. However, the stochastic nature of these interfacial waves occasionally causes wave 1 to fall into the separation region upstream of wave 2. This decreases both the drag coefficient and wave speed for wave 1 compared to wave 2, causing wave 2 to overtake wave 1 and merge the two waves into one larger wave that protrudes even further into the vapor flow as clearly depicted in Fig. 5(a). The newly established large wave acquires an even larger drag coefficient and moves faster than the previous individual waves. This large wave is now able to overtake more of the downstream smaller waves, acquiring more liquid mass and momentum. This process is believed to be responsible for the appreciable film thickening and large waves observed on the underside of the stainless steel tube.

Fig. 6 shows images of the condensation film for three narrow ranges of water mass velocity of G_w = 634.5–636.6, 845.5–854.2 and 1058.1–1063.0 kg/m^2 s and five FC-72 mass velocities of G = 33.7, 49.1, 65.7, 82.9 and 115.7 kg/m^2 s. Overall, the flow patterns are similar for equal FC-72 mass velocities despite the large

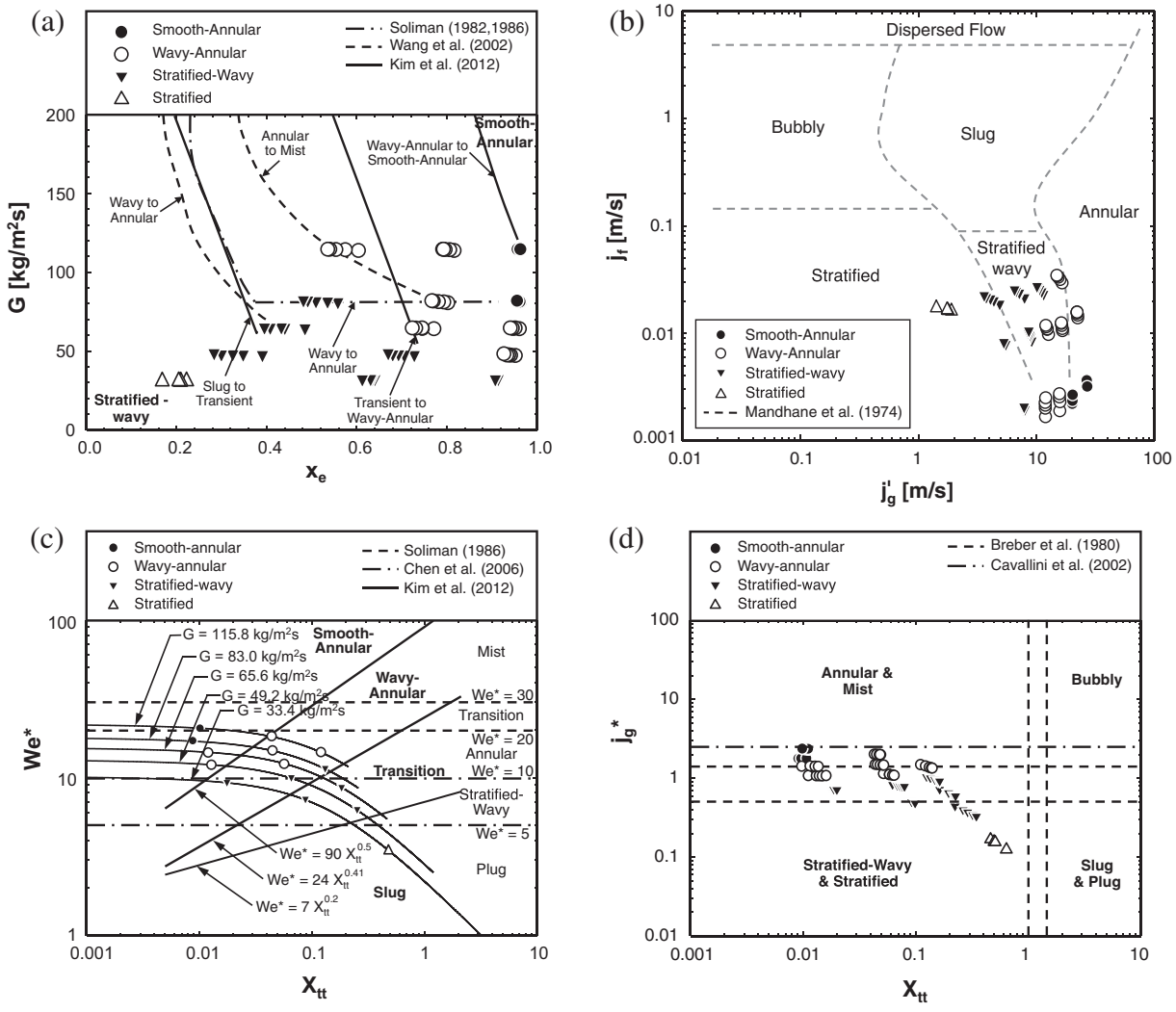

Fig. 7. Comparison of present flow regimes with flow regime maps of: (a) Soliman (1982, 1986), Wang et al. (2002) and Kim et al. (2012), (b) Mandhane et al. (1974), (c) Soliman (1986), Chen et al. (2006) and Kim et al. (2012), and (d) Breber et al. (1980) and Cavallini et al. (2002).

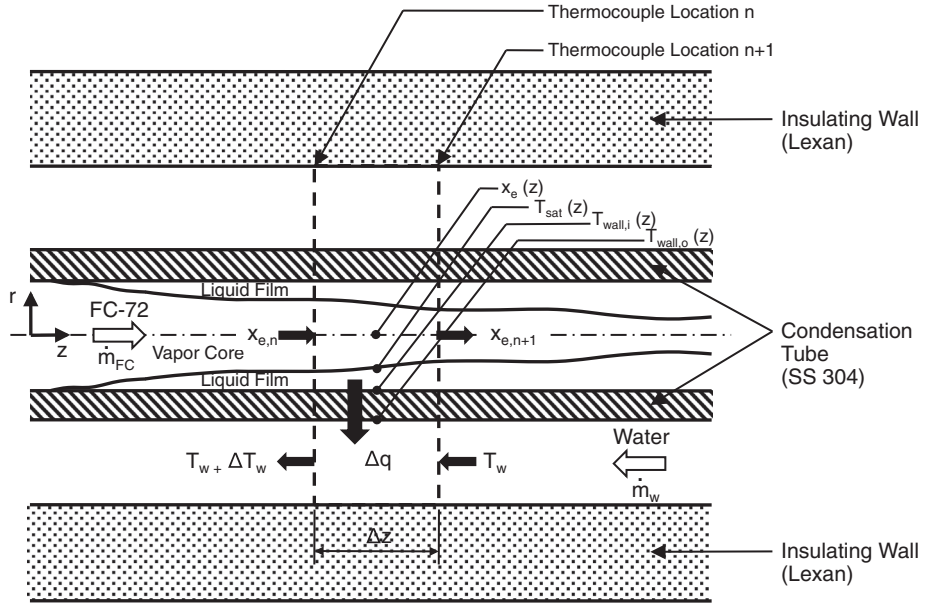

Fig. 8. Thermal model used to determine axial variations of heat transfer parameters.

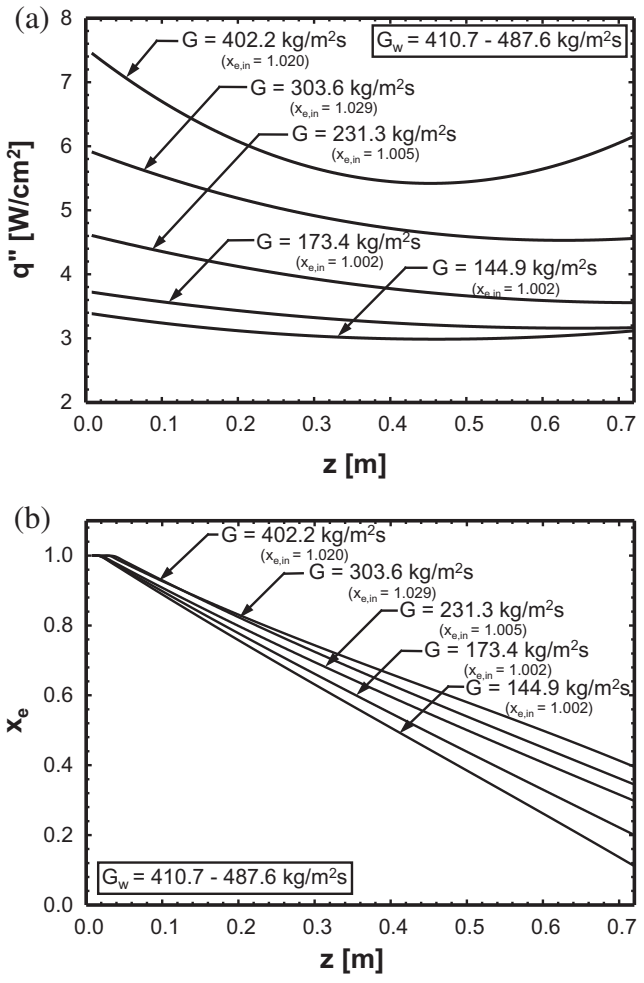

Fig. 9. Variations of (a) heat flux and (b) thermodynamic equilibrium quality along the condensation length for different FC-72 mass velocities.

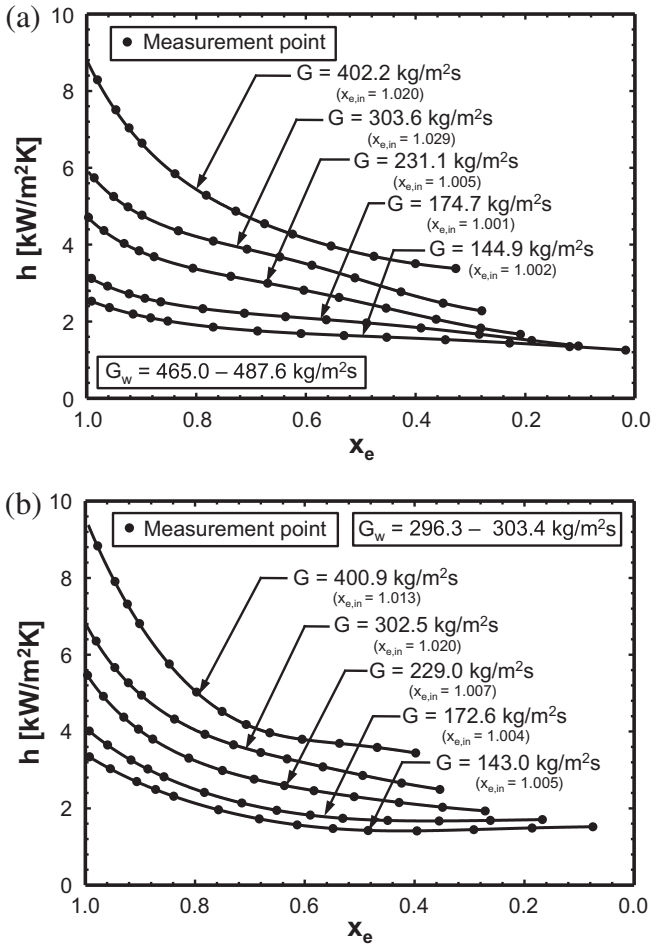

Fig. 10. Variations of experimentally-determined local condensation heat transfer coefficient with quality for different FC-72 mass velocities and water mass velocities in the ranges of (a) G_w = 465.0–487.6 kg/m^2 s, and (b) G_w = 296.3–303.4 kg/m^2 s.

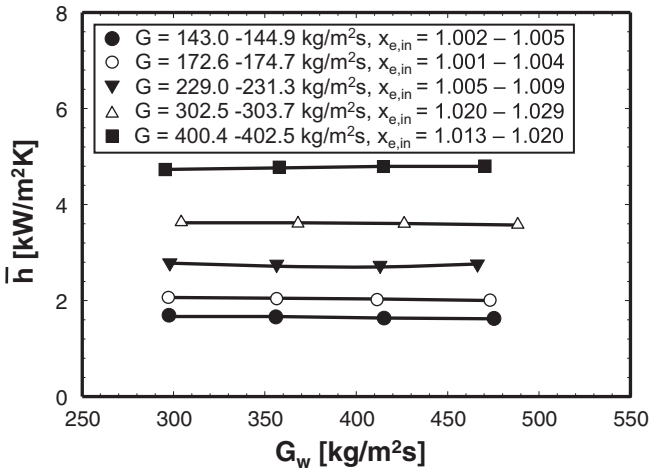

Fig. 11. Variation of experimentally-determined average condensation heat transfer coefficient with water mass velocity for different FC-72 mass velocities.

difference in the water mass velocities. This points to a liquid film's interfacial behavior far more sensitive to G than G_W. One reason for the relatively weak influence of G_w in the present study is the use of relatively high G_w values, which is intended to minimize the waterside thermal resistance in pursuit of reduced uncertainty in determining the FC-72 condensation heat transfer coefficient.

3.2. Assessment of flow regime maps

The experimental flow regime data are compared to four different types of flow regime maps. Table 2 provides details concerning working fluid, hydraulic diameter and quality range of these maps. Fig. 7(a) shows a comparison of the present flow regimes with mass velocity versus quality regime maps [17,23,24,40]. Despite differences in fluid type and channel size and geometry between the present study and those the maps are based upon, the maps do provide fair agreement in regime trends. Notice how a combination of high G and high x_e (*i.e.*, near the inlet) produces *smooth-annular* and *wavy-annular* regimes. This can be explained by these conditions greatly increasing the magnitude of vapor shear on the film interface. Increasing G also extents the *smooth-annular* and *wavy-annular* regimes to lower x_e values because of the increased vapor shear. On the other extreme, very low G values greatly reduce vapor shear, especially for small x_e, allowing gravity to play a dominant role in the form of *stratified* flow.

Fig. 7(b) compares the present flow regime data with the Mandhane et al. [25] map, which is based on the relationship between the superficial liquid and vapor velocities. Mandhane et al. constructed this map using 1178 of air–water data points. Later, Dobson and Chato [26] modified the Mandhane et al. map to achieve better agreement for refrigerants by replacing j_g with $j_g^* = \sqrt{\rho_g/\rho_{air}}j_g$, which accounts for the large density differences between air and refrigerant vapor. Fig. 7(b) shows the present *stratified-wavy* and *stratified* data are predicted with fair accuracy by the Mandhane et al. map modified per Dobson and Chato. However, the *smooth-annular* and *wavy-annular* data are observed at lower j_g values than predicted by the map. One reason for this departure is the relatively large hydraulic diameters used by Mandhane et al. Dobson and Chato pointed out that smaller diameters shift the transition line between *smooth-annular* and *wavy-annular* flows on one hand and *stratified-wavy* flow on the other to lower qualities, which correspond to lower superficial vapor velocities.

The experimental flow regime data are compared to two other types of regime maps that compensate for differences in working fluid and tube geometry with the aid of appropriate dimensionless groups. Fig. 7(c) compares the present data with those of Soliman [23,24], Chen et al. [41] and Kim et al. [40]. Soliman derived flow regime boundary relations by balancing destructive and stabilizing forces using a modified Weber number, We^*, and the Lockhart–Martinelli parameter, X_{tt}.

$$We^* = 2.45Re_g^{0.64}\left(\frac{\mu_g^2}{\rho_g\sigma D}\right)^{0.3}\Big/\phi_g^{0.4} \text{ for } \mathrm{Re}_f \leqslant 1250, \tag{1a}$$

$$\text{and} \quad We^* = 0.85Re_g^{0.79}\left(\frac{\mu_g^2}{\rho_g\sigma D}\right)^{0.3}\left[\left(\frac{\mu_g}{\mu_f}\right)^2\left(\frac{\rho_f}{\rho_g}\right)\right]^{0.084}\left(\frac{X_{tt}}{\phi_g^{2.55}}\right)^{0.157} \text{for } Re_f > 1250, \tag{1b}$$

$$\text{where} \quad Re_g = x_eGD/\mu_g, \tag{2a}$$

$$Re_f = G(1-x_e)D/\mu_f, \tag{2b}$$

$$X_{tt} = \left(\frac{1-x_e}{x_e}\right)^{0.9}\left(\frac{\rho_g}{\rho_f}\right)^{0.5}\left(\frac{\mu_f}{\mu_g}\right)^{0.1}, \tag{3}$$

$$\text{and} \quad \phi_g = 1 + 1.09X_{tt}^{0.039}. \tag{4}$$

Using Soliman's dimensionless groups, Chen et al. [41] recommended relations for the boundaries between *annular* and *stratified-wavy* regimes and between *stratified-wavy* and *plug* regimes based on experimental data for horizontal condensation of R134a inside 12 and 14-mm microfin tubes. Also using Soliman's dimensionless groups, Kim and Mudawar [42] recently proposed the following boundary relations:

$$Smooth-annular \text{ to } wavy-annular: \quad We^* = 90X_{tt}^{0.5}, \tag{5a}$$

$$Wavy-annular \text{ to } transition: \quad We^* = 24X_{tt}^{0.41}, \tag{5b}$$

$$Transition \text{ to } slug: \quad We^* = 7X_{tt}^{0.2}. \tag{5c}$$

Fig. 7(c) shows fair agreement between the present data and previous predictions. However, *stratified* flow is observed in the present study at G = 33.5–33.8 kg/m^2 s and x_e = 0.16–0.22 instead of the *slug* flow regime. This departure may be attributed to the unique annular geometry used in the present study.

Fig. 7(d) compares the present flow regime data to a flow regime map of dimensionless superficial vapor velocity, j_g^*, versus X_{tt}, where

$$j_g^* = \frac{x_eG}{\sqrt{gD\rho_g(\rho_f-\rho_g)}}. \tag{6}$$

Breber et al. [43] proposed *annular* flow is achieved for $j_g^* > 1.5$ and $X_{tt} < 1.0$, and *stratified* and *stratified-wavy* flow for and $X_{tt} < 1.0$. Cavallini et al. [28], on the other hand, recommended using $j_g^* > 2.5$ for *annular* flow and $j_g^* < 2.5$ for *intermittent* and *slug* flows. Because most of the present data lie in a transition region of the Breber et al. map, it is difficult to make any definitive inferences concerning the predictive accuracy of the map. Nonetheless, it should be noted that the boundary between *annular* and *stratified* flows falls exactly in transition region.

Overall, the present flow regime data show fair agreement with prior predictions utilizing the four different types of regime maps. However, the reader is reminded about the fundamental weakness of all regime maps, which stems from the inability to accurately describe boundaries between drastically different flow regimes

that are characterized by different dimensionless groups using a single two-dimensional plot.

4. Heat transfer results from CM-HT

4.1. Data reduction method

The local condensation heat transfer coefficient is obtained by discretizing the condensation length of the condensation module for heat transfer measurements, CM-HT, into small segments and using the relation

$$h(z) = \frac{q''(z)}{T_{sat}(z) - T_{wall,i}(z)}, \tag{7}$$

where $q''(z)$ is the local heat flux on the inner wall (FC-72 side) of the stainless steel tube in CM-HT, which, as illustrated in Fig. 8, is obtained from the local differential sensible heat rise of the cooling water, and related to the temperature difference and thermal resistance across the stainless steel wall.

$$q''(z) = \frac{\dot{m}_w c_{p,w} \Delta T_w(z)}{\pi D_i \Delta z} = \frac{T_{wall,i}(z) - T_{wall,o}(z)}{\frac{D_i \ln(D_o/D_i)}{2k_{ss}}} \tag{8}$$

With the inlet of the condensation length always maintained in superheated vapor state, the equilibrium quality is determined according to

$$x_e = 1 + \frac{c_{p,g}(T_g - T_{sat})}{h_{fg}} \text{ for } x_e \geqslant 1, \tag{9a}$$

and

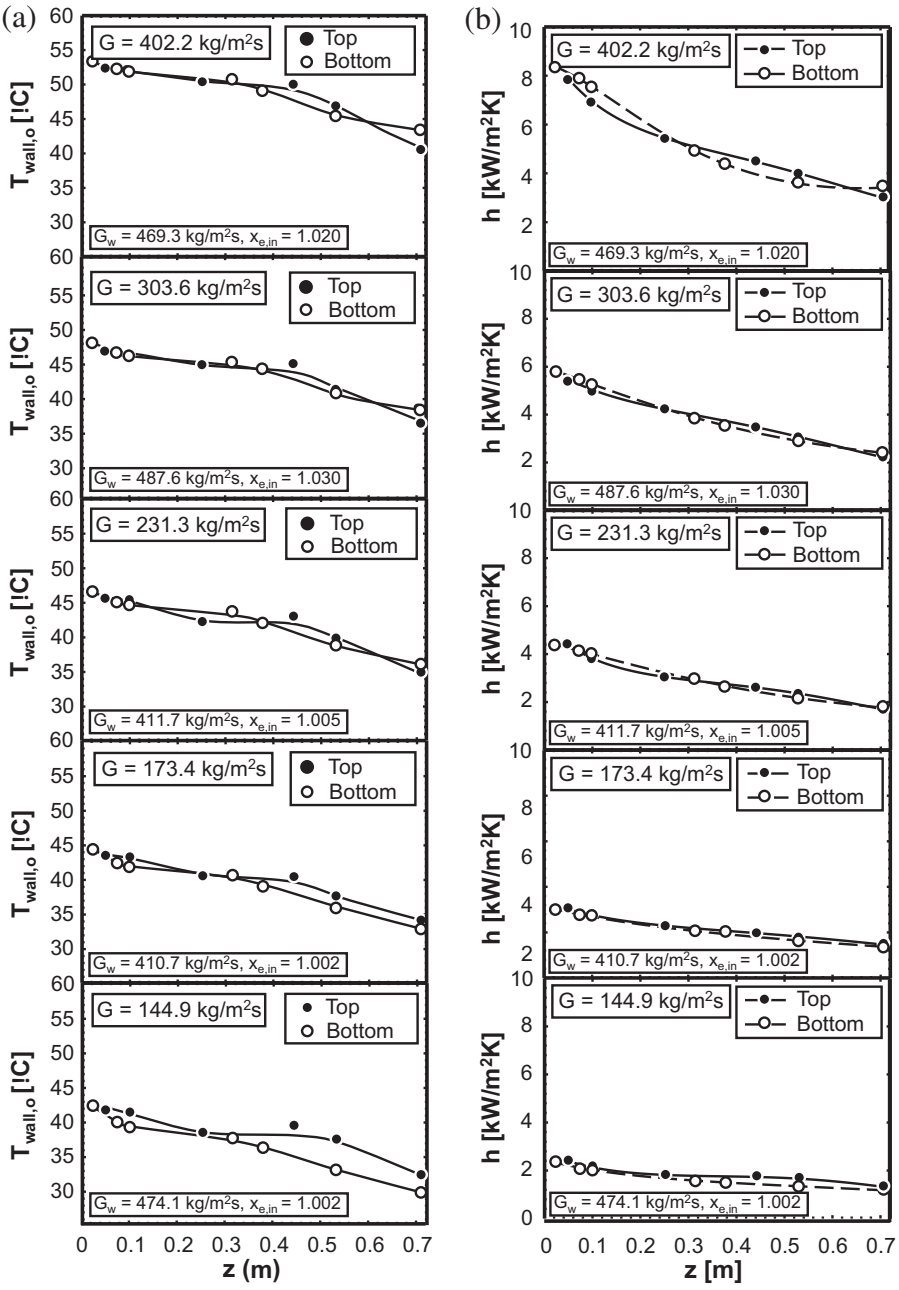

Fig. 12. Variations of (a) outer wall temperatures of stainless steel tube and (b) condensation heat transfer coefficients measured in CM-HT by top and bottom thermocouples for five FC-72 mass velocities.

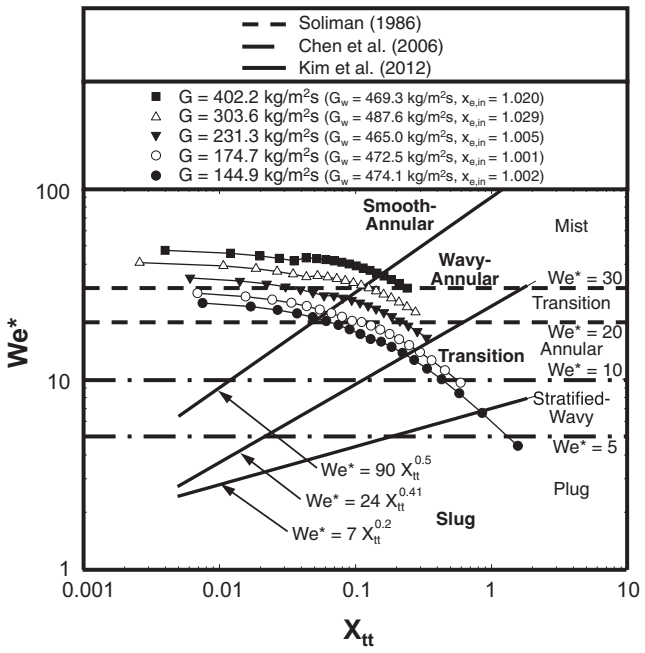

Fig. 13. Data from CM-HT superimposed with prior flow regime map predictions.

$$x_e = \frac{\dot{m} - \dot{m}_f}{\dot{m}} \text{ for } 0 < x_e < 1. \tag{9b}$$

where $\dot{m}_f$ is total condensate liquid flow rate, which is calculated according to

$$\dot{m}_f(z) = \sum_{i=1}^{n} \frac{\Delta q_i}{h_{fg}} \tag{10}$$

4.2. Axial variations of heat transfer parameters

Fig. 9(a) and (b) show, for five values of FC-72 mass velocity, axial variations of the wall heat flux along the inner wall (FC-72 side) of the stainless steel tube in CM-HT and the thermodynamic equilibrium quality, respectively, which are calculated from the measurements as discussed in the previous section. Fig. 10(a) and (b) show variations of the local heat transfer coefficient with local quality for two narrow ranges of water mass velocity of G_w = 465.0–487.6 kg/m^2 s and 296.3–303.4 kg/m^2 s, respectively. The heat transfer coefficient is highest near the inlet, where x_e is close to unity and the film thinnest, and decreases along the condensation length with decreasing x_e. For all values of G in Fig. 10(a) and (b), the decrease in h with decreasing x_e (*i.e.*, increasing axial distance) is very steep near the inlet, where the film is laminar and heat transfer dominated by conduction across the film. Farther downstream, however, the decrease in h is weaker because of emergence of turbulence in the liquid film, aided by the aforementioned growth of interfacial waves. Notice in Fig. 10(a) and (b) that these influences are far more pronounced for the highest FC-72 mass velocities than the lowest. Overall, h is shown increasing with increasing G because of the film thinning at higher vapor shear and increased turbulence intensity and waviness at high mass velocities.

Fig. 11 shows the variation of the condensation heat transfer coefficient averaged over the entire condensation length, excluding both the superheated inlet and subcooled downstream regions, with water mass velocity for different FC-72 mass velocities. The heat transfer coefficient displays high dependence on G compared to very weak dependence on G_w due to aforementioned reliance on high G_w values to minimize waterside thermal resistance and enhance accuracy in determining the FC-72 condensation heat transfer coefficient.

4.3. Circumferential variations of heat transfer parameters

It should be noted that calculations used to determine the axial variations of q'', x_e and h in CM-HT are obtained by circumferentially averaging the outer wall temperature of the stainless steel tube at each axial thermocouple station. Fig. 12(a) and (b) shows axial variations of the outer wall temperature of the stainless steel tube and condensation heat transfer coefficient, respectively, obtained from measurements by the top and bottom outer wall thermocouples for five different FC-72 mass velocities. Overall, differences are quite small except for the downstream region, especially for the low mass velocities, which are most susceptible to gravity effects. But unlike the flow in CM-FV, the condensate in CM-HT is confined along the stainless steel tube and is not able to drain below.

4.4. Determination of flow patterns in CM-HT

Fig. 13 shows the experimental data from CM-HT for five FC-72 mass velocities plotted in the flow regime map based on formulations by Soliman [23,24], Chen et al. [41] and Kim et al. [40]. It shows the present data are mostly in the *smooth-annular* and *wavy-annular* regions, excepting a few data points for the two lowest mass velocities.

4.5. Assessment of heat transfer correlations

Fig. 14(a)–(e) compare variations of the experimentally-determined local condensation heat transfer coefficient, h, with thermodynamic equilibrium quality, x_e, for five FC-72 mass velocities to predictions of 12 popular and recent correlations that are detailed in Table 3. The correlations can be categorized into three different types.

Correlations belonging to the first type, which include Haraguchi et al. [47], Wang et al. [17], Koyama et al. [48], Huang et al. [49], Park et al. [50] and Kim and Mudawar [20], are based on the Lockhart–Martinelli parameter. These correlations show a sharp increase in h near x_e = 1 because the Lockhart–Martinelli parameter, which is given by Eq. (3), is present in the denominator of these correlations. A sharp increase in h near x_e = 1 is actually observed in the present measurements at high FC-72 mass velocities, especially G = 303.6 kg/m^2 s, Fig. 14(d), and 402.2 kg/m^2 s, Fig. 14(e). The heat transfer coefficient is expected to be highest near x_e = 1 because this corresponds to the axial location where the film is thinnest. However, the measured increase is less pronounced than predicted by the correlations. Additionally, the sharp increase is not encountered for small FC-72 mass velocities, where h shows a nearly linear variation with x_e. The Dobson and Chato correlation [26] shows a linear trend over the entire range of x_e because the Lockhart–Martinelli parameter appears in both the numerator and dominator of this correlation. With a mean absolute error of MAE = 2.7%, this formulation shows best predictions of the present experimental data, where

$$MAE = \frac{1}{N} \sum \left| \frac{\bar{h}_{pred} - \bar{h}_{exp}}{\bar{h}_{exp}} \right|. \tag{11}$$

The correlation of Wang et al. highly overpredicts the data over the entire quality range. The correlations of Haraguchi et al. and Huang et al. underpredict the data in the high quality range of x_e = 0.6–0.8, and overpredict for x_e < 0.4. Overall, both correlations show good predictive capability, with MAEs of 6.6% and 6.1%, respectively.

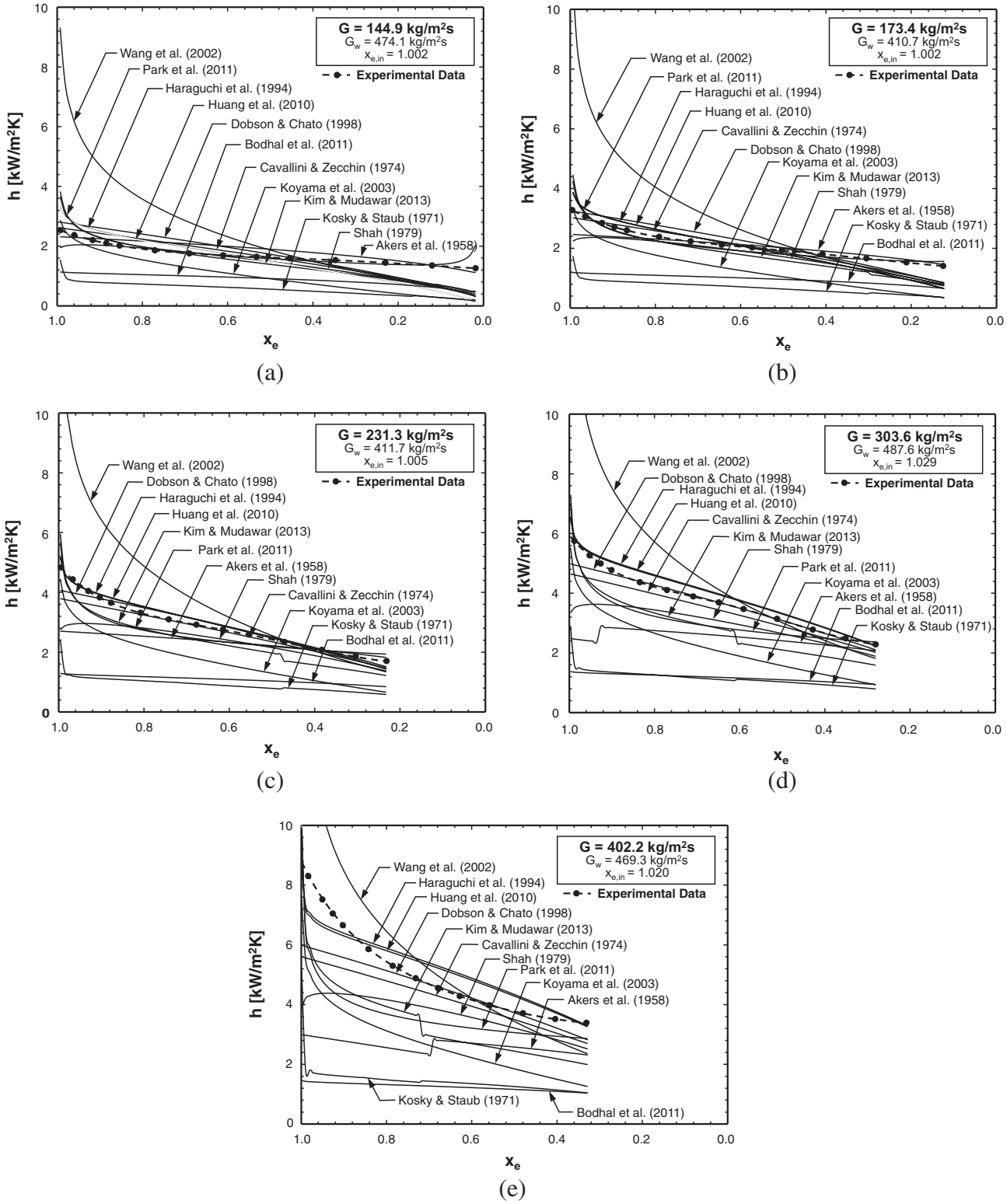

Fig. 14. Comparison of quality dependence of experimentally-determined local condensation heat transfer coefficient with predictions of prior correlations for (a) $G = 144.9$ kg/m^2 s, (b) $G = 173.4$ kg/m^2 s, (c) $G = 231.3$ kg/m^2 s, (d) $G = 303.6$ kg/m^2 s, and (e) $G = 402.2$ kg/m^2 s.

Correlations belonging to the second type do not use the Lockhart–Martinelli parameter. They predict a fairly linear trend in h for the entire range of x_e between 1 and 0 [15,44,46,51]. While these correlations do not capture the upstream increase in h, they do provide fairly good predictions of the data. It should be noted that some of these correlations use the average of inlet and outlet qualities to determine the local heat transfer coefficient, which explains why they do not capture the large upstream increase in h.

The analytical approach by Kosky and Staub [45] constitutes a third type of techniques for predicting the local heat transfer

Table 3
Condensation heat transfer correlations.

Author(s)	Correlation	Remarks
Akers et al. [44]	$\frac{hD_h}{k_f} = 0.0265Re_{eq}^{0.8}Pr_f^{1/3}$ for $Re_{eq} > 50,000$ $\frac{hD_h}{k_f} = 5.035Re_{eq}^{1/3}Pr_f^{1/3}$ for $Re_{eq} \leqslant 50,000$	$Re_{eq} = G\left[(1-x) + x\left(\frac{\rho_f}{\rho_g}\right)^{1/2}\right]\frac{D_h}{\mu_f}$ x is substituted with x_e in comparison
Kosky and Stuab [45]	$\frac{hD_h}{k_f} = \frac{1}{T^+}\frac{\rho_f c_{p,f} D_h v^*}{k_f}$	$v^* = \sqrt{\frac{-D_h}{4\rho_f}\left(\frac{dp}{dz}\right)_{fr}}$ $T^+ = \delta^+ Pr_f$ for $\delta^+ \leqslant 5$ $T^+ = 5\left[Pr_f + \ln(1 + Pr_f(\delta^+/5 - 1))\right]$ for $5 < \delta^+ \leqslant 30$ $T^+ = 5\left[Pr_f + \ln(1 + 5Pr_f) + 0.495\ln(\delta^+/30)\right]$ for $\delta^+ > 30$ where $\delta^+ = \sqrt{Re_f/2}$ for $Re_f \leqslant 1000$ and $\delta^+ = 0.0504Re_f^{7/8}$ for $Re_f > 1000$ x is substituted with x_e in comparison
Cavallini and Zecchin [46]	$\frac{hD_h}{k_f} = 0.05\left[Re_g\left(\frac{\mu_g}{\mu_f}\right)\left(\frac{\rho_f}{\rho_g}\right)^{0.5} + Re_f\right]^{0.8} Pr_f^{0.33}$	x is substituted with x_e in comparison
Shah [15]	$\frac{hD_h}{k_f} = 0.023Re_{fo}^{0.8}Pr_f^{0.4}\left[(1-x_e)^{0.8} + \frac{3.8x^{0.76}(1-x_e)^{0.04}}{P_R^{0.38}}\right]$	$Re_{fo} = \frac{GD_h}{\mu_f}$
Haraguchi et al. [47]	$\frac{hD_h}{k_f} = 0.0152(1 + 0.6Pr_f^{0.8})\left(\frac{\phi_g}{X_{tt}}\right)Re_f^{0.77}$	$\phi_g = 1 + 0.5\left(\frac{G}{\sqrt{gD_h\rho_g(\rho_f-\rho_g)}}\right)^{0.75} X_{tt}^{0.35}$
Dobson and Chato [26]	$\frac{hD_h}{k_f} = 0.023Re_f^{0.8}Pr_f^{0.4}\left[1 + \frac{2.22}{X_{tt}^{0.89}}\right]$	x is substituted with x_e in comparison
Wang et al. [17]	$\frac{hD_h}{k_f} = 0.0274Pr_f Re_f^{0.6792} x_e^{0.2208}\left(\frac{1.376 + 8X_{tt}^{1.655}}{X_{tt}^2}\right)^{0.5}$	x is substituted with x_e in comparison
Koyama et al. [48]	$\frac{hD_h}{k_f} = 0.0152(1 + 0.6Pr_f^{0.8})\left(\frac{\phi_g}{X_{tt}}\right)Re_f^{0.77}$	$\phi_g = 1 + 21(1 - e^{-0.319D_h})X_{tt} + X_{tt}^2 x$ is substituted with x_e in comparison
Huang et al. [49]	$\frac{hD_h}{k_f} = 0.0152(-0.33 + 0.83Pr_f^{0.8})\left(\frac{\phi_g}{X_{tt}}\right)Re_f^{0.77}$	$\phi_g = 1 + 0.5\left(\frac{G}{\sqrt{gD_h\rho_g(\rho_f-\rho_g)}}\right)^{0.75} X_{tt}^{0.35}$
Park et al. [50]	$\frac{hD_h}{k_f} = 0.0055Re_f^{0.7}Pr_f^{1.37}\frac{\phi_g}{X_{tt}}$;	$\phi_g^2 = 1 + 13.17\left(\frac{\rho_g}{\rho_f}\right)^{0.17}(1 - \exp\left(-0.6\sqrt{Bo}\right))X_{tt} + X_{tt}^2$, $Bo = \frac{g(\rho_f-\rho_g)D_h^2}{\sigma}$
Bohdal et al. [51]	$\frac{hD_h}{k_f} = 25.084Re_f^{0.258}Pr_f^{-0.495}P_R^{-0.288}\left(\frac{x_e}{1-x_e}\right)^{0.266}$;	
Kim and Mudawar [20]	$\frac{hD_h}{k_f} = 0.048Re_f^{0.69}Pr_f^{0.34}\frac{\phi_g}{X_{tt}}$;	$\phi_g^2 = 1 + CX + X^2$, $X^2 = \frac{(dP/dz)_f}{(dP/dz)_g}$ Different correlations for C for different laminar and turbulent liquid and vapor flow states

$Re_g = \frac{GxD_h}{\mu_g}$, $Re_f = \frac{G(1-x)D_h}{\mu_f}$, $X_{tt} = \left(\frac{1-x}{x}\right)^{0.9}\left(\frac{\rho_g}{\rho_f}\right)^{0.5}\left(\frac{\mu_f}{\mu_g}\right)^{0.1}$, $P_R = \frac{P}{P_{crit}}$

coefficient. However, this approach highly underpredicts the data for the entire range of FC-72 mass velocities, evidenced with a MAE of 68.4%.

Fig. 15 compares the experimentally-determined average condensation heat transfer coefficient with predictions of prior correlations, excepting those of Kosky and Stuab [45] and Bohdal et al. [51], which showed large MAEs of 68.4% and 63.6%, respectively.

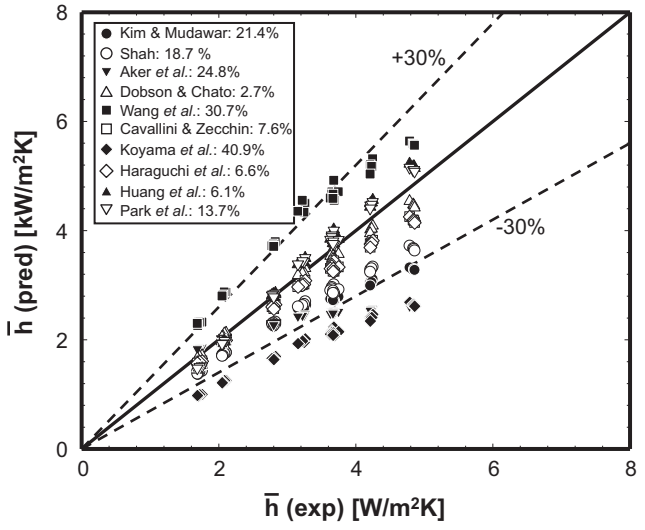

Fig. 15. Comparison of experimentally-determined average condensation heat transfer coefficient with predictions of prior correlations.

With the exception of Wang et al. [17] and Koyama et al. [48], all the correlations in Fig. 15 provide good to excellent predictions, with the correlation by Dobson and Chato [26], as indicated above, yielding the best MAE of 2.7%.

5. Conclusions

This study explored condensation heat transfer in horizontal channels. Two separate condensation modules were tested using FC-72 as working fluid. The first module, CM-HT, provided detailed heat transfer measurements of the condensing flow, and the second, CM-FV, was dedicated to video capture of the condensation film. Experimental data for the local and average condensation heat transfer coefficients were compared to predictions of recent and popular correlations. Key findings from the study are as follows.

(1) Four dominant flow regimes were identified: smooth-annular, wavy-annular, stratified-wavy and stratified. The boundaries between the different flow regimes show fair agreement with four different types of flow regime maps. Where waves are encountered, the film interface displays an array of small ripples and larger waves. The large waves appear to merge with one another into larger waves having greater liquid mass, amplitude and speed. The potentially important influence of waves on the motion and heat transfer behavior of the condensation film warrants more attention in future studies.

(2) The local condensation heat transfer coefficient is a strong function of the mass velocity of FC-72, and is highest near the inlet where quality is near unity and the film is thinnest, and decreases monotonically along the axial direction in

response to the film thickening. For high FC-72 mass velocities, the peak heat transfer coefficient in the inlet is very pronounced but the axial decrease in the downstream region slows significantly because of the combined effects of turbulence and increased interfacial waviness. For low FC-72 mass velocities, the variation of the local heat transfer coefficient is fairly linear over the entire range of quality.

(3) The experimental data for both the local and average condensation heat transfer coefficients show fairly good agreement with a number of popular and recent correlations. Correlations that utilize the Lockhart–Martinelli parameter show better prediction of the large peak values of the local condensation heat transfer coefficient near the inlet. A correlation by Dobson and Chato shows the best predictive capability of all the correlations tested, evidenced by a MAE of 2.7%.

Acknowledgement

The authors are grateful for the support of the National Aeronautics and Space Administration (NASA) under grant no. NNX13AB01G.

References

[1] I. Mudawar, Two-phase micro-channel heat sinks: theory, applications and limitations, J. Electron. Packaging – Trans. ASME 133 (2011). 041002-2.
[2] T.M. Anderson, I. Mudawar, Microelectronic cooling by enhanced pool boiling of a dielectric fluorocarbon liquid, J. Heat Transfer – Trans. ASME 111 (1989) 752–759.
[3] I. Mudawar, A.H. Howard, C.O. Gersey, An analytical model for near-saturated pool boiling CHF on vertical surfaces, Int. J. Heat Mass Transfer 40 (1997) 2327–2339.
[4] R.A. DeBortoli, S.J. Green, B.W. LeTourneau, M. Troy, A. Weiss, Forced-Convection Heat Transfer Burn-out Studies for Water in Rectangular and Round Tubes at Pressures above 500 psia, WAPD-188, Westinghouse Electric Corp., Pittsburgh, PA, 1958.
[5] T.C. Willingham, I. Mudawar, Forced-convection boiling and critical heat flux from a linear array of discrete heat sources, Int. J. Heat Mass Transfer 35 (1992) 2879–2890.
[6] M. Monde, T. Inoue, Critical heat flux in saturated forced convective boiling on a heated disk with multiple impinging jets, J. Heat Transfer – Trans. ASME 113 (1991) 722–727.
[7] D.C. Wadsworth, I. Mudawar, Enhancement of single-phase heat transfer and critical heat flux from an ultra-high-flux-source to a rectangular impinging jet of dielectric liquid, J. Heat Transfer – Trans. ASME 114 (1992) 764–768.
[8] M.E. Johns, I. Mudawar, An ultra-high power two-phase jet-impingement avionic clamshell module, J. Electronic Packaging – Trans. ASME 118 (1996) 264–270.
[9] L. Lin, R. Ponnappan, Heat transfer characteristics of spray cooling in a closed loop, Int. J. Heat Mass Transfer 46 (2003) 3737–3746.
[10] M. Visaria, I. Mudawar, Theoretical and experimental study of the effects of spray orientation on two-phase spray cooling and critical heat flux, Int. J. Heat Mass Transfer 51 (2008) 2398–2410.
[11] R.L. Webb, The evolution of enhanced surface geometries for nucleate boiling, Heat Transfer Eng. 2 (1981) 46–69.
[12] V. Khanikar, I. Mudawar, T. Fisher, Effects of carbon nanotube coating on flow boiling in a micro-channel, Int. J. Heat Mass Transfer 52 (2009) 3805–3817.
[13] M.K. Sung, I. Mudawar, Experimental and numerical investigation of single-phase heat transfer using a hybrid jet-impingement/micro-channel cooling scheme, Int. J. Heat Mass Transfer 49 (2006) 682–694.
[14] M.K. Sung, I. Mudawar, Correlation of critical heat flux in hybrid jet impingement/micro-channel cooling scheme, Int. J. Heat Mass Transfer 49 (2006) 2663–2672.
[15] M.M. Shah, A general correlation for heat transfer during film condensation inside pipes, Int. J. Heat Mass Transfer 22 (1979) 547–556.
[16] Y.Y. Yan, T.F. Lin, Condensation heat transfer and pressure drop of refrigerant R-134a in a small pipe, Int. J. Heat Mass Transfer 42 (1999) 697–708.
[17] W.-W. Wang, T.D. Radcliff, R.N. Christensen, A condensation heat transfer correlation for millimeter-scale tubing with flow regime transition, Exp. Thermal Fluid Sci. 26 (2002) 473–485.
[18] N.H. Kim, J.P. Cho, J.O. Kim, B. Youn, Condensation heat transfer of R-22 and R-410A in flat aluminum multi-channel tubes with or without micro-fins, Int. J. Refrig. 26 (2003) 830–839.
[19] S.M. Kim, I. Mudawar, Universal approach to predicting two-phase frictional pressure drop for adiabatic and condensing mini/micro-channel flows, Int. J. Heat Mass Transfer 55 (2012) 3246–3261.
[20] S.M. Kim, I. Mudawar, Universal approach to predicting heat transfer coefficient for condensing mini/micro-channel flow, Int. J. Heat Mass Transfer 56 (2013) 238–250.
[21] W. Qu, I. Mudawar, Flow boiling heat transfer in two-phase micro-channel heat sinks-II. Annular two-phase flow model, Int. J. Heat Mass Transfer 46 (2003) 2773–2784.
[22] I. Park, S.M. Kim, I. Mudawar, Experimental measurement and modeling of downflow condensation in a circular tube, Int. J. Heat Mass Transfer 57 (2013) 567–581.
[23] H.M. Soliman, The mist-annular transition during condensation and its influence on the heat transfer mechanism, Int. J. Multiphase Flow 12 (1986) 277–288.
[24] H.M. Soliman, On the annular-to-wavy flow pattern transition during condensation inside horizontal tubes, Can. J. Chem. Eng. 60 (1982) 475–481.
[25] J.M. Mandhane, G.A. Gregory, K. Aziz, A flow pattern map for gas—liquid flow in horizontal pipes, Int. J. Multiphase Flow 1 (1974) 537–553.
[26] M.K. Dobson, J.C. Chato, Condensation in smooth horizontal tubes, J. Heat Transfer – Trans. ASME 120 (1998) 193–213.
[27] R.G. Sardesai, R.G. Owen, D.J. Pulling, Flow regimes for condensation of a vapour inside a horizontal tube, Chem. Eng. Sci. 36 (1981) 1173–1180.
[28] A. Cavallini, G. Censi, D.D. Col, L. Doretti, G.A. Longo, L. Rossetto, Condensation of halogenated refrigerants inside smooth tubes, HVAC&R Res. 8 (2002) 429–451.
[29] W.S. Bousman, A.E. Dukler, Studies of gas–liquid flow in microgravity: void fraction, pressure drop and flow patterns, AMD-174/FED-175, in: Proc. Symposium on Fluid Mechanics Phenomena in Microgravity, ASME Winter Annual Meeting, New Orleans, LA, 1993, pp. 23–36.
[30] L. Zhao, S. Rezkallahk, Pressure drop in gas–liquid flow at microgravity conditions, Int. J. Multiphase Flow 21 (1995) 837–849.
[31] H. Zhang, I. Mudawar, M.M. Hasan, Flow boiling CHF in microgravity, Int. J. Heat Mass 48 (2005) 3107–3118.
[32] H. Han, K.S. Gabriel, The influence of flow pressure gradient on interfacial wave properties in annular two-phase flow at microgravity and normal gravity conditions, Fluid Dyn. Mater. Process. 2 (2006) 287–295.
[33] X. Fang, Y. Xu, Correlations for two-phase friction pressure drop under microgravity, Int. J. Heat Mass Transfer 56 (2013) 594–605.
[34] I. Mudawar, R.A. Houpt, Mass and momentum transport in smooth falling liquid films laminarized at relatively high Reynolds numbers, Int. J. Heat Mass Transfer 36 (1993) 3437–3448.
[35] I. Mudawar, R.A. Houpt, Measurement of mass and momentum transport in wavy-laminar falling liquid films, Int. J. Heat Mass Transfer 36 (1993) 4151–4162.
[36] J.A. Shmerler, I. Mudawar, Local heat transfer coefficient in wavy free-falling turbulent liquid films undergoing uniform sensible heating, Int. J. Heat Mass Transfer 31 (1988) 67–77.
[37] T.H. Lyu, I. Mudawar, Statistical investigation of the relationship between interfacial waviness and sensible heat transfer to a falling liquid film, Int. J. Heat Mass Transfer 34 (1991) 1451–1464.
[38] T.H. Lyu, I. Mudawar, Determination of wave-induced fluctuations of wall temperature and convective heat transfer coefficient in the heating of a turbulent falling liquid film, Int. J. Heat Mass Transfer 34 (1991) 2521–2534.
[39] J.A. Shmerler, I. Mudawar, Local evaporative heat transfer coefficient in turbulent free-falling liquid films, Int. J. Heat Mass Transfer 31 (1988) 731–742.
[40] S.M. Kim, J. Kim, I. Mudawar, Flow condensation in parallel micro-channels–Part 1: experimental results and assessment of pressure drop correlations, Int. J. Heat Mass Transfer 55 (2012) 971–983.
[41] Q. Chen, R.S. Amano, M. Xin, Experimental study of flow patterns and regimes of condensation in horizontal three-dimensional micro-fin tubes, Heat Mass Transfer 43 (2006) 201–206.
[42] S.M. Kim, I. Mudawar, Flow condensation in parallel micro-channels. Part 2: heat transfer results and correlation technique, Int. J. Heat Mass Transfer 55 (2012) 984–994.
[43] G. Breber, J. Palen, J. Taborek, Prediction of horizontal tube-size condensation of pure components using flow regime criteria, J. Heat Transfer – Tran. ASME 102 (1980) 471–476.
[44] W.W. Akers, H.A. Deans, O.K. Crosser, Condensing heat transfer within horizontal tubes, Chem. Eng. Progress 54 (1958) 89–90.
[45] P.G. Kosky, F.W. Staub, Local condensing heat transfer coefficients in the annular flow regime, AIChE J. 17 (1971) 1037–1043.
[46] A. Cavallini, R. Zecchin, A dimensionless correlation for heat transfer in forced convection condensation, in: Proc. 5th Int. Heat Transfer Conf., Tokyo, Japan, 3, 1974, pp. 309–313.
[47] H. Haraguchi, S. Koyama, T. Fujii, Condensation of refrigerants HCFC 22, HFC 134a and HCFC 123 in a horizontal smooth tube (2nd report), Trans. JSME (B) 60 (1994) 245–252.
[48] S. Koyama, K. Kuwahara, K. Nakashita, K. Yamamoto, An experimental study on condensation of refrigerant R134a in a multi-port extruded tube, Int. J. Refrig. 24 (2003) 425–432.
[49] X. Huang, G. Ding, H. Hu, Y. Zhu, H. Peng, Y. Gao, B. Dengo, Influence of oil on flow condensation heat transfer of R410A inside 4.18 mm and 1.6 mm inner diameter horizontal smooth tubes, Int. J. Refrig. 33 (2010) 158–169.
[50] J.E. Park, F. Vakili-Farahani, L. Consolini, J.R. Thome, Experimental study on condensation heat transfer in vertical minichannels for new refrigerant R1234ze(E) versus R134a and R236fa, Exp. Therm. Fluid Sci. 35 (2011) 442–454.
[51] T. Bohdal, H. Charun, M. Sikora, Comparative investigations of the condensation of R134a and R404A refrigerants in pipe minichannels, Int. J. Heat Mass Transfer 54 (2011) 1963–1974.